RSC Advances

PAPER

View Article Online
View Journal | View Issue

Cite this: *RSC Adv.*, 2022, **12**, 207

$Co_2O_3/Co_2N_{0.67}$ nanoparticles encased in honeycomb-like N, P, O-codoped carbon framework derived from corncob as efficient ORR electrocatalysts†

Yanling Wu, *[a] Qinggao Hou,[a] Fangyuan Qiu,[a] Meili Qi,[a] Cuicui Sun[a] and Yanli Chen *[b]

Received 19th September 2021
Accepted 13th December 2021

DOI: 10.1039/d1ra07017g

rsc.li/rsc-advances

It is essential to develop cost-effective rechargeable metal–air batteries, with high activity, stability, and efficiency, that use non-precious metals (NPMs)-based cathodic oxygen reduction reaction (ORR) catalysts. Here, by using earth-abundant corncob (CC) as the carbon source, $Co(OH)_2$, NaH_2PO_4, and melamine as the precursors, and KOH as the chemical activator, CoNP@bio-C-a is obtained and comparative studies are carried out with three other types of CC-derived carbon-based catalytic materials, namely, bio-C, CoP@bio-C, and CoNP@bio-C. Depending mainly on the formation of $Co_2O_3/Co_2N_{0.67}$ active sites (as p–n heterojunctions) and N, P, O-containing functional groups, the resultant CoNP@bio-C-a catalyst exhibits best electrocatalytic activity among the four types of catalysts; *via* a 4-electron pathway, it has good stability and good methanol tolerance. In addition, its unique honeycomb-like porous structure, high graphitization degree, and abundant oxygen-containing groups contribute to its excellent ORR activity. This study provides insights for exploring the application of heteroatom-doped biomass-derived carbon catalysts.

1. Introduction

In the field of fuel cells and rechargeable metal–air batteries, it is essential to explore high-efficiency oxygen reduction reaction (ORR) electrocatalysts; however, their applications are affected by the rate-limiting processes in cathodic ORR.[1,2] Pt-based catalysts are contemporary commonly used commercial catalysts. However, they have disadvantages, such as inactivation after poisoning, poor stability, high cost, and limited availability.[3] Hence, exploring efficient and stable non-precious metal (NPM)-based ORR catalysts would be beneficial for energy conversion systems.

Biomass has attracted considerable attention because it is abundant and inexpensive. Biomass-derived carbon-based materials also have good electrical conductivities and high specific surface areas and porosities, along with three-dimensional morphologies. However, biomass-based carbon materials are not ideal ORR electrocatalysts. Heteroatom-doped biomass-based porous carbon materials have drawn considerable attention owing to their promising ORR activities.[4] Introducing heteroatoms (such as N, P, S, B, and O) into the carbon framework causes carbon defects by modification of the surface electronic structures and/or changing the polarity of the carbon framework for generating active sites.[5–7] Studies have demonstrated that the introduction of heteroatoms (such as P, S, B, and O) into N-doped carbon materials can further improve the ORR performance.[8] Phosphorus and nitrogen have similar electronic structures; phosphorus can change the charge density of materials by its lone pair of electrons in the 3p orbital and attract the lone pairs in O_2 in its empty 3d orbital.[9,10] Hence, phosphorus has better capacity to supply electrons. The oxygen atom has high electronegativity, and so, O-doping can not only adjust the electronic structure of carbon materials, but also enhance their hydrophilicities, and thus, accelerate the ORR activity.[11] In recent years, ternary heteratomic doping has attracted considerable attention because of its synergistic effect

[a]*School of Transportation and Civil Engineering, Shandong Jiaotong University, Ji'nan 250357, China. E-mail: wuyanling621@163.com*

[b]*College of Science, China University of Petroleum (East China), Qingdao 266580, China*

† Electronic supplementary information (ESI) available: Supplementary data related to this article are available with the online version of this paper. Correspondence and requests regarding these materials can be addressed to Y.-l. Wu. The supplementary file contains the following data: EDS mapping images, FT-IR and Raman spectra, Mott–Schottky plots and amperometric *i–t* curves of CoNP@bio-C-a; LSV curves of bio-C, CoP@bio-C, CoNP@bio-C, and CoNP@bio-C-a; CV and LSV curves CoP@bio-C-a, N@bio-C-a, CoNP@bio-C-a-700, CoNP@bio-C-a-900, and CoNP@bio-C-a-N_2; SEM images and N_2 adsorption/desorption isotherms of CoNP@bio-C-a-700 and CoNP@bio-C-a-900; PXRD patterns, SEM images, and high-resolution XPS curves of the Co 2p, O 1s, and P 2p core levels of CoNP@bio-C-a before and after stability tests; contact angle measurements of bio-C, CoP@bio-C, CoNP@bio-C, CoNP@bio-C-a, and N@bio-C-a. See DOI: 10.1039/d1ra07017g

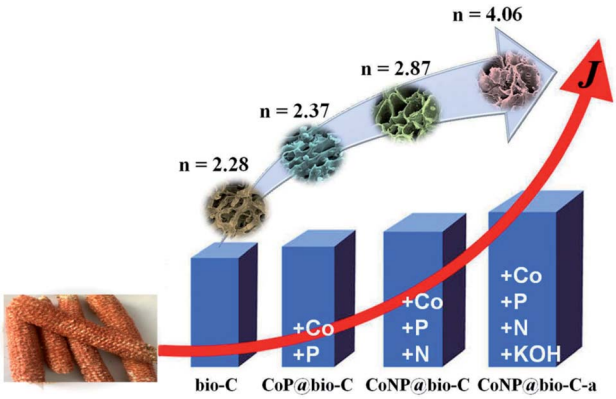

Fig. 1 Schematic illustration of the synthesis of four types of carbon-based catalytic materials (*n* is the electron transfer number).

on improving the ORR activity of carbon materials. However, there are relatively few reports on oxygen ternary doping in carbon materials.[12]

Herein, a new honeycomb-like porous carbon hybrid with Co, N, P, O-codoping (denoted as CoNP@bio-C-a) is prepared from waste biomass (corncob, CC) mixed with cobalt hydroxide, sodium hypophosphite, and melamine (precursors) and KOH (activating agent) through a simple one-step pyrolysis process. The resultant CoNP@bio-C-a catalyst exhibits a 4-electron process, contains active sites from $Co_2O_3/Co_2N_{0.67}$ hetero-junctions and N, P, O-codoped carbon, and shows excellent electroactivity, good stability, and methanol resistance in 0.1 M KOH ($E_{onset} = 0.92$ V, $E_{1/2} = 0.85$ V, $J_L = -5.5$ mA cm^{-2}).

2. Experimental section

2.1. Samples preparation for doped and undoped bio-C materials

Cleaned and dried CC was milled at 300 rpm. CC powder (5.7 g), $Co(OH)_2$ (0.05 g), and $NaH_2PO_2 \cdot H_2O$ (0.25 g) were mixed in deionized water and subjected to ultrasound. The product was dried and then mixed with melamine (precursor) with a mass ratio of 2 : 1 and grinded till it was mixed uniformly. Then, KOH powder (0.2 g) was added to this mixture and grinded till it was mixed uniformly. The obtained CoNP@bio-C-a was first carbonized in an inert atmosphere of 10 °C min^{-1} at 500 °C for 2 h and then activated using CO_2 gas at 800 °C for 3 h. The obtained mixture was cooled, cleaned, and dried. For comparison, the CC-based porous carbon material (bio-C), $Co(OH)_2$–$NaH_2PO_2 \cdot H_2O$ precursor-doped CC-based porous carbon (CoP@bio-C), $Co(OH)_2$–$NaH_2PO_2 \cdot H_2O$–KOH precursor-doped CC-based porous carbon (CoP@bio-C-a), $Co(OH)_2$–$NaH_2PO_2 \cdot H_2O$–melamine precursor-doped CC-based porous carbon (CoNP@bio-C), and melamine-KOH precursor-doped CC-based porous carbon (N@bio-C-a) were prepared under the same conditions used for the preparation of CoNP@bio-C-a, as shown in Fig. 1.

Characterization and electrochemical measurement methods are described in ESI.†

3. Results and discussion

3.1. Morphological and structural characterization

Morphologies of bio-C, CoP@bio-C, CoNP@bio-C, and CoNP@bio-C-a were visualized using scanning electron microscopy (SEM, Fig. 2). The SEM images revealed the improvement of the pore structures from undoped bio-C, CoP@bio-C, and CoNP@bio-C to CoNP@bio-C-a. With the introduction of Co and P into the bio-C framework (Fig. 2a and b), the pore size of the fibrous network structure in bio-C decreased from approximately 40 μm for bio-C to 10 μm for CoP@bio-C. After incorporating Co, N, and P into the bio-C framework, an ordered honeycomb structure (diameter = 10–20 μm, wall thickness = 600 nm) was obtained (Fig. 2c). Fig. 2d shows no obvious morphological changes during the conversion of CoNP@bio-C to CoNP@bio-C-a, but it shows that uniform pores (size = ~2 μm) appeared on the relatively thick walls of the honeycomb-like structure of CoNP@bio-C-a.

The microstructure of CoNP@bio-C-a was examined using high-resolution transmission electron microscopy (HRTEM) (Fig. 3). Some small inorganic spots (diameters = 5–11 nm) were encased in the carbon layers (Fig. 3a), indicating the presence of the active species of Co_2O_3 and $Co_2N_{0.67}$ in the carbon materials (Fig. 3b and c). The values of *d*-spacing were 0.39, 0.18, and 0.20 nm, assigned to the (002) plane of graphite carbon, (100) plane of Co_2O_3, and (101) plane of $Co_2N_{0.67}$ in CoNP@bio-C-a, respectively.[13] EDX spectra reveal (Fig. S1†) the atomic percentage composition of Co : P as approximately 3 : 8 = 0.375 (0.24 : 0.83). The inductively coupled plasma optical emission spectrometry (ICP-OES) results (Table S1†) show that the atomic composition of CoNP@bio-C-a in an aqua regia solution is 7 : 18 = 0.389 (0.73 : 1.81), which matched well with the findings of EDX analysis. This confirms that these two elements

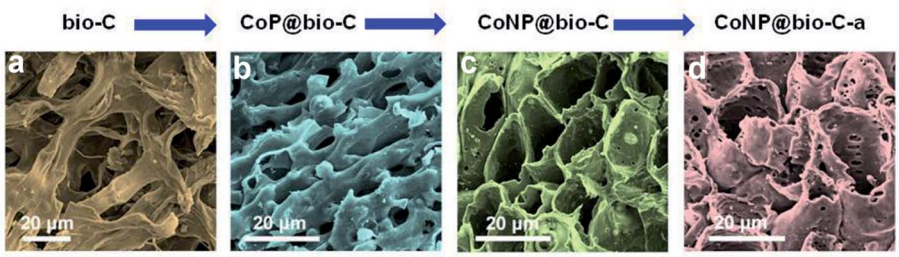

Fig. 2 Representative SEM images of (a) bio-C, (b) CoP@bio-C, (c) CoNP@bio-C, and (d) CoNP@bio-C-a.

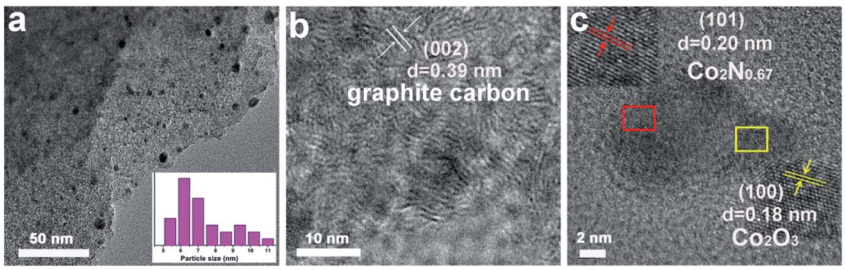

Fig. 3 (a) TEM image of CoNP@bio-C-a (inset: particle size distribution of CoNP@bio-C-a); lattice fringe images of (b) graphitic carbon and (c) $Co_2N_{0.67}$ and Co_2O_3 from the HRTEM image of CoNP@bio-C-a.

were successfully incorporated into the material.[14,15] The elemental mapping images (Fig. S2†) further show that Co, C, P, N, and O were evenly distributed in CoNP@bio-C-a.

The crystal structures of bio-C, CoP@bio-C, CoNP@bio-C, and CoNP@bio-C-a, were evaluated using PXRD (Fig. 4a). The prepared samples had a wide (002) diffraction peak at ~22° and an observable (101) diffraction characteristic at ~44°, showing that the graphite structure was disordered and mainly an sp^2 hybrid structure was observed, which is in good agreement with the HRTEM and Raman results.[16] Closer inspection revealed that the diffraction peak of the (002) plane from graphitic carbon (GC) of bio-C, CoP@bio-C, and CoNP@bio-C shifted only slightly at 2θ values of 22.07° (0.402 nm), 22.09° (0.402 nm), and 21.91° (0.405 nm), respectively. After KOH activation, the GC (002) diffraction peak of CoNP@bio-C-a moved to a higher angle ($2\theta = 22.88°$, $d_{002} = 0.388$ nm) with a smaller d-spacing compared to that of CoNP@bio-C, implying a stronger layer-to-layer (*i.e.*, π–π) interaction in the GC framework in CoNP@bio-C-a.[17–19] The weak diffraction peaks in the PXRD patterns indicate that nanoparticles of $Co_2N_{0.67}$ (JCPDS no. 06-0691) and Co_2O_3 (JCPDS no. 02-0770) are present in CoNP@bio-C-a. Raman spectra of bio-C, CoP@bio-C, CoNP@bio-C, and CoNP@bio-C-a (Fig. 4b) displayed two peaks at approximately 1330 cm^{-1} and 1590 cm^{-1}, respectively. The GC phase exists in biological-based carbon materials.[20] The I_D/I_G values for bio-C (1.26), CoP@bio-C (1.27), and CoNP@bio-C (1.26) were similar; however, it decreased to 1.24 for CoNP@bio-C-a. Consequently, both the lowest I_D/I_G (1.24) and the smallest layer-spacing (0.388 nm) for CoNP@bio-C-a among the four types of samples, including doped and undoped bio-C materials, unraveled the relatively high graphitization degree of CoNP@bio-C-a, which should be expected to reduce the barrier for charge transfer.[21,22] In addition, several weak signal peaks were detected in the low wavelength range of the Raman spectra, indicating the presence of cobalt oxide in CoNP@bio-C-a (Fig. S3, ESI†).[23] To further investigate the specific surface areas of doped and undoped bio-C samples, nitrogen adsorption–desorption isotherms were measured (Fig. 4c and Table S2, ESI†). The BET specific surface areas of the four types of samples were compared and revealed a clear trend toward higher specific surface areas, following the order CoP@bio-C (291.82 $m^2\ g^{-1}$) < CoNP@bio-C (365.40 $m^2\ g^{-1}$) < bio-C (455.74 $m^2\ g^{-1}$) < CoNP@bio-C-a (475.55 $m^2\ g^{-1}$). The large accessible surface area of CoNP@bio-C-a is beneficial for electrolyte penetration and oxygen adsorption, which can positively impact the electrocatalytic activity, as discussed below.[24] In contrast, CoP@bio-C and CoNP@bio-C exhibited slightly low BET surface areas, which may be caused by the excessive corrosion and distortion due to Co, N, P-codoping into the bio-C structure.[25]

X-ray photoelectron spectroscopy (XPS) measurements of CoNP@bio-C-a were used to characterize the surface compositions and chemical valence states (Fig. 5). The survey spectra revealed distinct peaks of C, Co, N, O, and P, with elemental contents of 71.28%, 9.02%, 1.09%, 17.58%, and 1.03%, respectively (Fig. 5a), showing that Co, P, N, and O were successfully doped in CoNP@bio-C-a. Particularly, the C 1s spectrum can be divided into four peaks centered at 284.8 (C=C), 285.6 (C=N/C–O/C–P), 286.5 eV (C=O/C–N), and 289.4 eV (O–C=O) (Fig. 5b). The high content of sp^2-carbon (C=C at 284.8 eV) further indicates the existence of GC, which enhances the electron conductivity of carbon materials, improving ORR

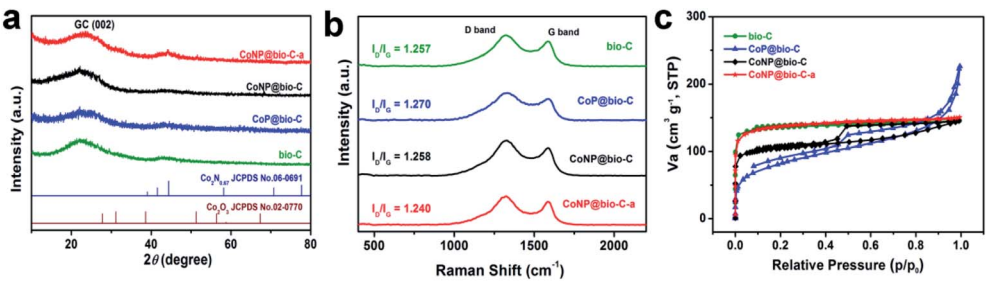

Fig. 4 (a) PXRD patterns; (b) Raman spectra; (c) N_2 adsorption/desorption isotherms of bio-C, CoP@bio-C, CoNP@bio-C, and CoNP@bio-C-a.

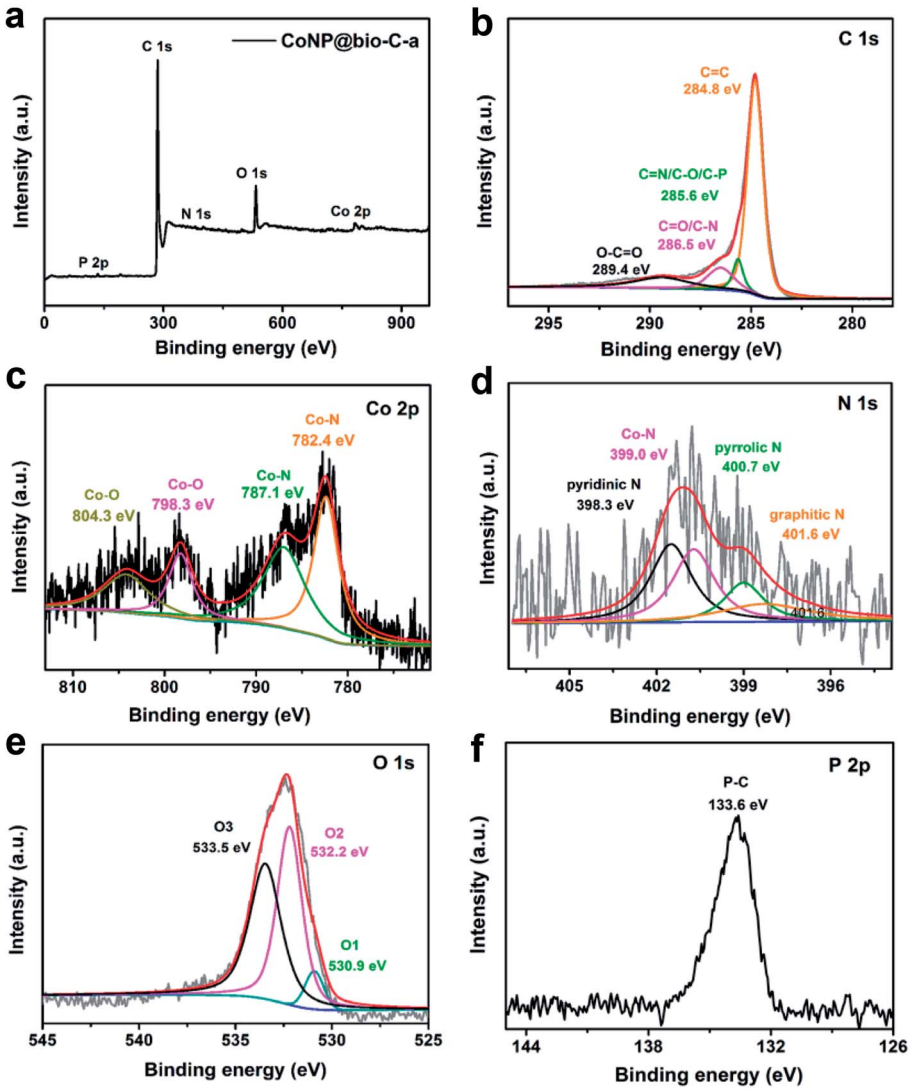

Fig. 5 (a) XPS survey spectra of CoNP@bio-C-a. High-resolution XPS spectra of (b) C 1s, (c) Co 2p, (d) N 1s, (e) O 1s, and (f) P 2p core levels for CoNP@bio-C-a.

activities.[26] The other three peaks of C 1s at 285.6, 286.5, and 289.4 eV are attributed to the defects and functional groups due to nitrogen and phosphorus heteroatom doping in the carbon matrix.[27,28] In the Co 2p spectra for CoNP@bio-C-a (Fig. 5c), the peaks at approximately 782.1 and 786.8 eV belong to Co–N species, while the peaks at 798.3 and 803.6 eV originate from Co–O species. Both Co–N and Co–O species also can improve the catalytic activity of ORR under alkaline conditions.[29] Moreover, some groups indicate that the N-rich porous carbon shell surrounding exposed Co_3O_4 particles improves the conductivity of the particles, which in turn increases the ORR activity.[30] The fitted N 1s spectra for CoNP@bio-C-a centered at 398.3, 399.0, 401.6, and 400.7 eV can be assigned to pyridinic, pyrrolic, and graphitic nitrogen and Co–N, respectively (Fig. 5d).[31,32] Studies have demonstrated that the incorporation of nitrogen and a metal as active centers in a carbon matrix can reduce the local work function on the carbon surface.[33–35] The deconvolution of the O 1s region of CoNP@bio-C-a (Fig. 5e) comprises peaks at 530.9 (O1), 532.2 (O2), and 533.5 eV (O3). The sharp peak at 530.9 eV is caused by the lattice oxygen (O^{2-}) of Co_2O_3. The peaks at 532.2 and 533.5 eV belong to the oxygen-containing functional groups on the carbon surface.[30] To qualitatively characterize the chemical functional groups, FTIR spectra of CoNP@bio-C-a were collected (Fig. S4, ESI†). The peaks near 1697, 1460, and 1133 (wide peak) cm^{-1} are attributed to C=O stretching vibration,[36] C=C and/or C=N bands,[37] and the C–O bond,[38] respectively. Three absorption bands are observed at 896, 1050, and 1280 cm^{-1}, which can be assigned to P–O–C or P=O–C stretching. The high-resolution P 2p peak for CoNP@bio-C-a was further verified using XPS analysis (Fig. 5f). The P 2p peak centered at 133.6 eV belongs to P–C bonds, indicating that P elements have been doped in the biomass-based carbon material.[39,40] These results show that Co, N, P, and O were successfully incorporated in CoNP@bio-C-a. Doping of nitrogen and oxygen in carbon materials can improve the

electrical conductivity and surface wettability, which is helpful for improving the electrochemical catalytic performance.[41]

3.2. Electrochemical properties

The ORR activity of the as-prepared carbon catalysts (bio-C, CoP@bio-C, CoNP@bio-C, and CoNP@bio-C-a) was assessed using cyclic voltammetry (CV) in a 0.1 M KOH solution (O_2-saturated: solid lines, N_2-saturated: dotted lines; Fig. 6a and Table S3, ESI†). Comparison of the CV profiles showed that CoP@bio-C and CoNP@bio-C demonstrated slightly improved ORR activity than bio-C. As expected, upon adding KOH activator in CoNP@bio-C, the resultant CoNP@bio-C-a exhibited enhanced catalytic ORR activity due to shifting of the peak potential to a more positive value ($E_{1/2}$ = 0.85 V), further confirming the effectiveness of the chemical activations of carbon materials in improving the catalytic activity of ORR.[42]

The ORR activities of the four types of carbon-based catalytic materials were further investigated using LSV polarization curves (Fig. 6b). For comparison, ORR activity of 20 wt% Pt/C for industrial use was studied. The ORR activity of all the doped biomass-based carbon materials was better than that of undoped bio-C (Fig. 6b, S5–S7, and Table S3, ESI†), and the order of ORR activities was bio-C (E_{onset} = 0.85 V, $E_{1/2}$ = 0.69 V, J_L = −2.78 mA cm^{-2}) < CoP@bio-C (E_{onset} = 0.85 V, $E_{1/2}$ = 0.79 V, J_L = −3.47 mA cm^{-2}) < CoNP@bio-C (E_{onset} = 0.89 V, $E_{1/2}$ = 0.82 V, J_L = −3.84 mA cm^{-2}) < CoNP@bio-C-a (E_{onset} = 0.92 V, $E_{1/2}$ = 0.85 V, J_L = −5.49 mA cm^{-2}), indicating that the treatment for the bio-C materials proceeded stepwise. However, the BET surface areas of CoP@bio-C and CoNP@bio-C were lower than that of bio-C-800 (Table S2, ESI†). Furthermore, to assess the contribution of the Co compound and carbon doping carbon on ORR, CoP@bio-C-a, N@bio-C-a, and NP@bio-C-a were prepared from CC powder by adding only auxiliary precursors of $Co(OH)_2$–$NaH_2PO_2 \cdot H_2O$–KOH, melamine–KOH, and $NaH_2PO_2 \cdot H_2O$–melamine–KOH, respectively. CV and LSV profiles were employed to study the ORR catalytic activity of CoP@bio-C-a (E_{onset} = 0.89 V, $E_{1/2}$ = 0.83 V, J_L = −3.77 mA cm^{-2}), N@bio-C-a (E_{onset} = 0.90 V, $E_{1/2}$ = 0.71 V, J_L = −3.06 mA cm^{-2}), and NP@bio-C-a (E_{onset} = 0.85 V, $E_{1/2}$ = 0.71 V, J_L = −3.06 mA cm^{-2}) in an O_2-saturated 0.1 M KOH electrolyte (Fig. S8–S10 and Table S3, ESI†), and they both displayed lower catalytic activity than CoNP@bio-C-a. For comparison, the catalytic activities of CoNP@bio-C-a generated *via* pyrolysis at 700 °C and 900 °C were also examined using CV and LSV profiles with the RDE configuration (Fig. S11, S12 and Table S3, ESI†). Pyrolysis temperatures lower or higher than 800 °C resulted in poor catalytic activity of ORR compared with CoNP@bio-C-a. This phenomenon was further analyzed using BET and SEM characterization. At 700 °C, it had a three-dimensional bowl-shaped structure; however, it had a small specific surface area due to the insufficient temperature of activated pore creation. At 900 °C, it had a large specific surface area; however, it did not maintain a good honeycomb structure during the activation process, resulting in fewer attachment points for the active sites (Fig. S13, S14 and Table S2, ESI†). In addition, the ORR measurements of CoNP@bio-C-a-N_2 in the N_2 process were compared with the corresponding results (summarized in Fig. S15 and Table S3, ESI†). Compared with the CO_2-activated CoNP@bio-C-a catalyst, the CoNP@bio-C-a-N_2 catalyst showed poor ORR catalytic properties (E_{onset} = 0.86 V, $E_{1/2}$ = 0.65 V) in

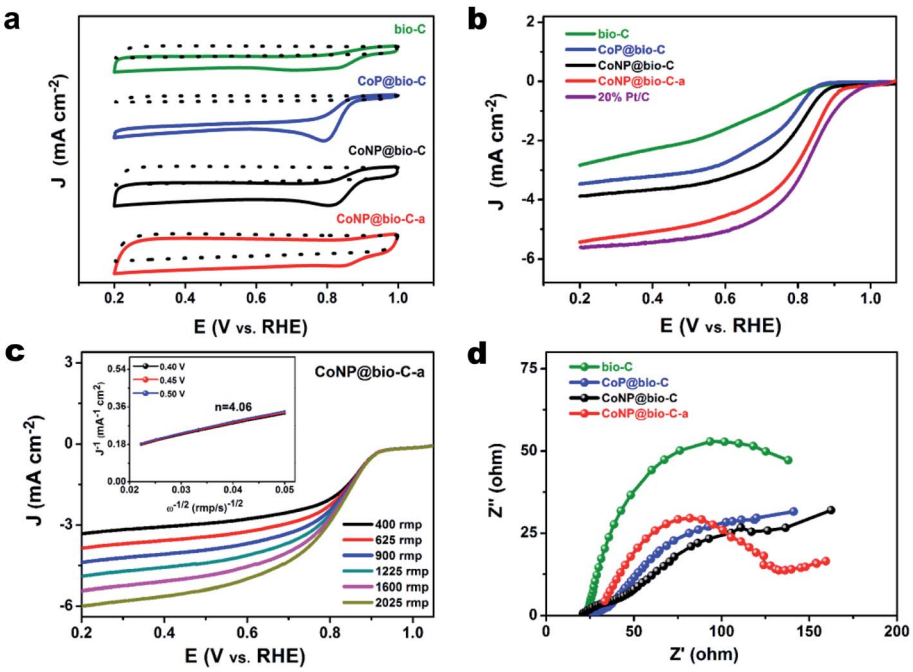

Fig. 6 (a) CVs of bio-C, CoP@bio-C, CoNP@bio-C, and CoNP@bio-C-a. (b) LSV curves of as-prepared catalysts and commercial 20 wt% Pt/C catalyst at 1600 rpm. (c) LSV curves of CoNP@bio-C-a at various values of revolutions per minute (inset: K–L plots of CoNP@bio-C-a). (d) Nyquist plots of bio-C, CoP@bio-C, CoNP@bio-C, and CoNP@bio-C-a catalysts-modified electrodes.

an O_2-saturated 0.1 M KOH solution. These results demonstrated that the CO_2 activation process has a positive influence on biomass-based carbon materials.[43] Consistent with the CV study, CoNP@bio-C-a displayed the best performance of ORR activity among the heteroatom-doped bio-C and undoped bio-C catalysts, that is, with $E_{onset} = 0.92$ V and $E_{1/2} = 0.85$ V (O_2-saturated 0.1 M KOH), which are comparable to the corresponding values of the commercial Pt/C catalyst ($E_{onset} = 0.96$ V, $E_{1/2} = 0.86$ V, $J_L = -5.61$ mA cm^{-2}).

To further understand the electron transfer ability of CoNP@bio-C-a, LSV tests were carried out at 400–2025 rpm; the results are shown in Fig. 6c. Typically, current density is enhanced upon increase in the rotation rate. The Koutecky–Levich (K–L) plots of CoNP@bio-C-a catalyst showed good linearity, which indicates a first-order reaction kinetics process under different potentials. The electron transfer number (n) for CoNP@bio-C-a at a potential range of 0.40–0.50 V was calculated to be approximately 4 (inset of Fig. 6c), with an average value of 3.94, indicating that the oxygen reduction process followed the 4-electron reduction process, which was similar to that of the Pt/C catalyst. Furthermore, electrochemical impedance spectroscopy (EIS) images of the four types of carbon-based catalytic materials were assessed. As shown in Fig. 6d, the smallest charge transfer resistance (R_t) of CoNP@bio-C-a obtained from the Nyquist plots indicates the beneficial role of the honeycomb-like structure and the $Co_2O_3/Co_2N_{0.67}$ nanoparticles encased in the N, P, O-codoped carbon framework. We also performed Mott–Schottky (M–S) analysis at an AC frequency of 10 Hz to investigate the conductivity of CoNP@bio-C-a (Fig. S16, ESI†). A typical inverted "V-shape" plot was obtained in the M–S plot of CoNP@bio-C-a, confirming the formation of p–n junctions.[44] To evaluate the impact of p–n junctions on ORR performance, the generated Co_2O_3 nanoparticles of the CoNP@bio-C-a were leached using an HCl solution. A positive slope (n-type) in the M–S plots appeared instead of the typical inverted "V-shape" plot of CoNP@bio-C-a (Fig. S17, ESI†). The LSV tests revealed that the ORR activity of the acid-treated samples decreased considerably ($E_{onset} = 0.90$ V, $E_{1/2} = 0.82$ V, $J_L = -3.88$ mA cm^{-2}) (Fig. S18, ESI†), which confirms the crucial role of the p–n junctions in ORR. Thus, the existence of p–n heterojunctions in CoNP@bio-C-a created sufficient space charge layers to improve the current generation, which facilitated interfacial electron transfer in the ORR.[45,46] This, combined with the change of the surface electronic structure of the carbon matrix because of the formation of C–P, C–N, and C–O active sites, led to the high ORR performance of CoNP@bio-C-a. Meanwhile, $Co_2O_3/Co_2N_{0.67}$ nanoparticles, as active sites encased within a honeycomb-like N, P, O-codoped carbon framework, further enhanced the ORR activity.

Long-term durability of ORR catalysts is generally examined using chronoamperometric responses. The stability of CoNP@bio-C-a and Pt/C at 1600 rpm under a high constant voltage of 0.8 V was measured (Fig. S19a, ESI†). For CoNP@bio-C-a, 73% of the initial current density was retained after continuous operation for 10 000 s, while for the Pt/C catalyst, rapid activity loss occurred, and it could retain only approximately 60% of the initial current density. Therefore, abundant nitrogen species may provide stable anchoring sites for Co-based active components and improve the stability of catalysts.[47–49] Furthermore, methanol crossover experiments revealed that when methanol was added to the solution, there was no significant influence on the current density of CoNP@bio-C-a. In contrast, the current of the Pt/C catalyst decreased significantly under methanol oxidation (Fig. S19b, ESI†). The internal composition and morphology of CoNP@bio-C-a were studied and analyzed after long-term stability tests. XRD patterns of CoNP@bio-C-a after durability tests showed no changes in its chemical composition, indicating that the catalyst composition was stable (Fig. S20, ESI†). In the XPS spectrum of Co 2p, the Co–O peak moved to a higher energy region, while the Co–N peak moved to a lower energy region. The initial sharp peaks of CoNP@bio-C-a for O 1s and P 2p at 532.4 eV and 133.6 eV moved toward higher energy regions, 532.5 eV and 134.2 eV, after the ORR durability test, and new peaks appeared at approximately 536.3 eV and 140.9 eV, likely attributed to the chemisorbed oxygen (Fig. S21, ESI†).[50] Samples of CoNP@bio-C-a were collected after the stability tests, and their SEM profiles showed that the honeycomb-like morphology of the catalyst was retained (Fig. S22, ESI†). These results indicate that CoNP@bio-C-a has good structural stability.

Surface wettability of electrocatalysts is an important factor.[51–53] Hence, we carried out surface wettability tests of the four materials. The contact angle decreased in the order bio-C (~72°) > CoP@bio-C (~73°) > CoNP@bio-C (~51°) > CoNP@bio-C-a (~46°), indicating that the treatment of the bio-C materials was followed by further functionalization in the above order (Fig. S23, ESI†). This contributed to the best ORR catalytic activity of CoNP@bio-C-a. The heteroatoms of Co, N, O, and P were also beneficial in enhancing the contact between the electrolyte and the electrode surface compared to that in the pure bio-C (~72°) and N-doped N@bio-C-a (~69°) electrodes, respectively (Fig. S23e, ESI†). The resulting enhanced affinity to H_2O is favorable for enhancing the catalytic activity of CoNP@bio-C-a toward ORR.

4. Conclusions

We explored a high-performance ORR catalyst, CoNP@bio-C-a, which was obtained using earth-abundant CC as the carbon source, sodium hypophosphite, melamine, and cobalt hydroxide as the precursors, and KOH as the chemical activator. This catalyst exhibited excellent electroactivity in 0.1 M KOH ($E_{onset} = 0.92$ V, $E_{1/2} = 0.85$ V, $J_L = -5.5$ mA cm^{-2}), which was superior to that of the commercial Pt/C catalyst. The high activities are attributed to the unique nanostructures of $Co_2O_3/Co_2N_{0.67}$ (as p–n junctions), heteratomic doping (Co, N, P, and O), and large specific surface areas. This study showed that high-performance electrocatalysts can be prepared from biomass derivatives through rational design.

Author contributions

Writing—original draft and writing—review & editing, Y. -l. W.; investigation, Q. -g. H.; data curation, F. -y. Q.; supervision, C. -c.

S.; funding acquisition, M. -l. Q.; resources, Y. -l. C. All authors have read and agreed to the published version of the manuscript.

Conflicts of interest

There are no conflicts to declare.

Acknowledgements

This work is financially supported by the Doctoral Scientific Research Foundation of Shandong Jiaotong University (BS50004952), the Transportation Department Foundation of Shandong Province (2021B118), and the Natural Science Foundation of Shandong Province (ZR2021MB027). The authors would like to thank MJEditor (http://www.mjeditor.com) for its linguistic assistance during the preparation of this manuscript.

References

1 N. Ma, Y. Jia, X. F. Yang, X. L. She, L. Z. Zhang, Z. Peng, X. D. Yao and D. J. Yang, Seaweed biomass derived (Ni,Co)/CNT nanoaerogels: Efficient bifunctional electrocatalysts for oxygen evolution and reduction reactions, *J. Mater. Chem. A*, 2016, **4**, 6376–6384.

2 Z. Y. Chen, Q. C. Wang, X. B. Zhang, Y. P. Lei, W. Hu, Y. Luo and Y. B. Wang, N-doped defective carbon with trace Co for efficient rechargeable liquid electrolyte-/all-solid-state Zn-air batteries, *Sci. Bull.*, 2018, **63**, 548–555.

3 J. C. Meier, C. Galeano, I. Katsounaros, A. A. Topalov, A. Kostka, F. Schüth and K. J. J. Mayrhofer, Degradation mechanisms of Pt/C fuel cell catalysts under simulated start-stop conditions, *ACS Catal.*, 2012, **2**, 832–843.

4 Y. H. Qian, I. A. Khan and D. Zhao, Electrocatalysts derived from metal–organic frameworks for oxygen reduction and evolution reactions in aqueous media, *Small*, 2017, **13**, 1701143.

5 B. Men, Y. Z. Sun, M. J. Li, C. Q. Hu, M. Zhang, L. N. Wang, Y. Tang, Y. M. Chen, P. Y. Wan and J. Q. Pan, Hierarchical metal-free nitrogen-doped porous graphene/carbon composites as an efficient oxygen reduction reaction catalyst, *ACS Appl. Mater. Interfaces*, 2016, **8**, 1415–1423.

6 Z. Wang, S. J. Peng, Y. X. Hu, L. L. Li, T. Yan, G. R. Yang, D. X. Ji, M. Srinivasane, Z. J. Pan and S. Ramakrishna, Cobalt nanoparticles encapsulated in carbon nanotube-grafted nitrogen and sulfur co-doped multichannel carbon fibers as efficient bifunctional oxygen electrocatalysts, *J. Mater. Chem. A*, 2017, **5**, 4949–4961.

7 G. Y. Ren, Y. N. Li, Q. S. Chen, Y. Qian, J. G. Zheng, Y. Zhu and C. Teng, Sepia-derived N, P co-doped porous carbon spheres as oxygen reduction reaction electrocatalyst and supercapacitor, *ACS Sustainable Chem. Eng.*, 2018, **6**, 16032–16038.

8 J. Y. Jin, H. M. Wu, S. F. Wang, Y. Yu Ding and S. Y. Yin, Heteroatoms doped C3N4 as high performance catalysts for the oxygen reduction reaction, *Int. J. Hydrogen Energy*, 2017, **42**, 20579–20588.

9 B. Zheng, J. Wang, Z. Pan, X. Wang, S. Liu, S. Ding and L. Lang, An efficient metal-free catalyst derived from waste lotus seedpod for oxygen reduction reaction, *J. Porous Mater.*, 2020, **27**, 637–646.

10 Z. Zhou, A. Chen, X. Fan, A. Kong and Y. Shan, Hierarchical porous N-P-coupled carbons as metal-free bifunctional electro-catalysts for oxygen conversion, *Appl. Surf. Sci.*, 2019, **464**, 380–387.

11 W. Ni, Y. Gao, Y. Zhang, H. A. Younus, X. Guo, C. Ma, Y. Zhang, J. Duan, J. Zhang and S. Zhang, O-doping boosts the electrochemical oxygen reduction activity of a single Fe site in hydrophilic carbon with deep mesopores, *ACS Appl. Mater. Interfaces*, 2019, **11**, 45825–45831.

12 Y. N. Li, J. Han, Z. L. Xu, R. F. Zhao, Y. Wang and R. Guo, N-, P-, and O-tridoped carbon hollow nanospheres with openings in the shell surfaces: A highly efficient electrocatalyst toward the ORR, *Langmuir*, 2021, **37**, 2001–2010.

13 H. Y. Jing, Y. T. Shi, X. D. Song, S. X. Liang, D. Y. Wu, Y. L. An and C. Hao, Dual sites of CoO nanoparticles and Co−Nx embedded within coal based support toward advanced triiodide reduction, *ACS Sustainable Chem. Eng.*, 2019, **7**, 10484–10492.

14 M. X. Chen, M. Z. Zhu, M. Zuo, S. Q. Chu, J. Zhang, Y. Wu, H. W. Liang and X. L. Feng, Identification of catalytic sites for oxygen reduction in metal/nitrogen-doped carbons with encapsulated metal nanoparticles, *Angew. Chem., Int. Ed.*, 2019, **59**, 1627–1633.

15 Y. C. Lin, P. Y. Liu, E. Velasco, G. Yao, Z. Q. Tian, L. J. Zhang and L. Chen, Fabricating single-atom catalysts from chelating metal in open frameworks, *Adv. Mater.*, 2019, 1808193.

16 B. B. Huang, Y. C. Liu and Z. L. Xie, Biomass derived 2D carbons *via* a hydrothermal carbonization method as efficient bifunctional ORR/HER electrocatalysts, *J. Mater. Chem. A*, 2017, **5**, 23481–23488.

17 P. Liu, Y. M. Li, Y. S. Hu, H. Li, L. Q. Chen and X. J. Huang, A waste biomass derived hard carbon as a high performance anode material for sodium-ion batteries, *J. Mater. Chem. A*, 2016, **4**, 13046–13052.

18 J. Guo, X. M. Yan, Q. Liu, Q. Li, X. Xu, L. T. Kang, Z. M. Cao, G. L. Chai, J. Chen, Y. B. Wang and J. N. Yao, The synthesis and synergistic catalysis of iron phthalocyanine and its graphene-based axial complex for enhanced oxygen reduction, *Nano Energy*, 2018, **46**, 347–355.

19 Y. N. Gong, D. L. Li, C. Z. Luo, Q. Fu and C. X. Pan, Highly porous graphitic biomass carbon as advanced electrode materials for supercapacitors, *Green Chem.*, 2017, **19**, 4132–4140.

20 W. Zhou, T. Xiong, C. Shi, J. Zhou, K. Zhou, N. Zhu, L. Li, Z. Tang and S. Chen, Bioreduction of precious metals by microorganism: Efficient gold@N-doped carbon electrocatalysts for the hydrogen evolution reaction, *Angew. Chem.*, 2016, **55**, 8416–8420.

21 H. K. Jeong, Y. P. Lee, R. J. Lahaye, M. H. Park, K. H. An, I. J. Kim, C. W. Yang, C. Y. Park, R. S. Ruoff and Y. H. Lee,

Evidence of graphitic AB stacking order of graphite oxides, *J. Am. Chem. Soc.*, 2008, **130**, 1362–1366.

22 J. Hou, C. Cao, F. Idrees and X. Ma, Hierarchical porous nitrogen-doped carbon nanosheets derived from silk for ultrahigh-capacity battery anodes and supercapacitors, *ACS Nano*, 2015, **9**, 2556–2564.

23 C. W. Tang, C. B. Wang and S. H. Chien, Characterization of cobalt oxides studied by FT-IR, Raman, TPR and TG-MS, *Thermochim. Acta*, 2008, **473**, 68–73.

24 X. J. Zheng, X. C. Cao, X. W. Li, J. H. Tian, C. Jin and R. Z. Yang, Biomass lysine-derived nitrogen-doped carbon hollow cubes *via* a NaCl crystal template: An efficient bifunctional electrocatalyst for oxygen reduction and evolution reactions, *Nanoscale*, 2017, **9**, 1059–1067.

25 X. Xu, S. J. You, L. Yang, Z. P. Xing, S. Y. Pan, Z. Cai, Y. Dai and J. L. Zou, Highly efficient charge transfer in Co/Co2P Schottky junctions embedded in nitrogen-doped porous carbon for enhancing bioelectricity generation, *Biosens. Bioelectron.*, 2018, **102**, 101–105.

26 K. L. Ai, Y. L. Liu, C. P. Ruan, L. H. Lu and G. Q. Lu, Sp2 C-dominant N-doped carbon sub-micrometer spheres with a tunable size: A versatile platform for highly efficient oxygen-reduction catalysts, *Adv. Mater.*, 2013, **25**, 998–1003.

27 H. H. Zhang, Y. P. Fan, B. Z. Liu, Y. Y. Liu, S. M. Ashraf, X. L. Wu, G. S. Han, J. Gao and B. J. Li, Birdcage-type CoOx-carbon catalyst derived from metal-organic frameworks for enhanced hydrogen generation, *ACS Sustainable Chem. Eng.*, 2019, **7**, 9782–9792.

28 H. Wu, J. Geng, H. T. Ge, Z. Y. Guo, Y. G. Wang and G. F. Zheng, Egg-derived mesoporous carbon microspheres as bifunctional oxygen evolution and oxygen reduction electrocatalysts, *Adv. Energy Mater.*, 2016, **6**, 1600794.

29 X. D. Wen, L. Bai, M. Li and J. Q. Guan, Atomically dispersed cobalt- and nitrogen-codoped graphene toward bifunctional catalysis of oxygen reduction and hydrogen evolution reactions, *ACS Sustainable Chem. Eng.*, 2019, **7**, 9249–9256.

30 J. Masa, W. Xia, I. Sinev, A. Q. Zhao, Z. Y. Sun, S. Grützke, P. Weide, M. Muhler and W. Schuhmann, MnxOy/NC and CoxOy/NC nanoparticles embedded in a nitrogen doped carbon matrix for high-performance bifunctional oxygen electrodes, *Angew. Chem., Int. Ed.*, 2014, **53**, 8508–8512.

31 Z. Zhang, J. H. Hao, W. S. Yang and J. L. Tang, Defect-rich CoP/nitrogen-doped carbon composites derived from a metal-organic framework: High performance electrocatalysts for the hydrogen evolution reaction, *ChemCatChem*, 2015, **7**, 1920–1925.

32 Y. J. Zhang, L. H. Lu, S. Zhang, Z. Z. Lv, D. T. Yang, J. H. Liu, Y. Chen, X. C. Tian, H. Y. Jin and W. G. Song, Biomass chitosan derived cobalt/nitrogen doped carbon nanotubes for the electrocatalytic oxygen reduction reaction, *J. Mater. Chem. A*, 2018, **6**, 5740–5745.

33 X. Zou, X. Huang, A. Goswami, R. Silva, B. R. Sathe, E. Mikmekova and T. Asefa, Cobalt-embedded nitrogen-rich carbon nanotubes efficiently catalyze hydrogen evolution reaction at all pH values, *Angew. Chem., Int. Ed.*, 2014, **53**, 4372–4376.

34 W. Zhou, J. Zhou, Y. Zhou, J. Lu, K. Zhou, L. Yang, Z. Tang, L. Li and S. Chen, N-doped carbon-wrapped cobalt nanoparticles on N-doped graphene nanosheets for high-efficiency hydrogen production, *Chem. Mater.*, 2015, **27**, 2026–2032.

35 W. Zhou, Y. Zhou, L. Yang, J. Huang, Y. Ke, K. Zhou, L. Li and S. Chen, N-doped carbon-coated cobalt nanorod arrays supported on a titanium mesh as highly active electrocatalysts for the hydrogen evolution reaction, *J. Mater. Chem. A*, 2015, **3**, 1915–1919.

36 Y. Ji, T. Li, L. Zhu, X. Wang and Q. Lin, Preparation of activated carbons by microwave heating KOH activation, *Appl. Surf. Sci.*, 2007, **254**, 506–512.

37 S. Zhang, W. Huang, P. Hu, C. Huang, C. Shang, C. Zhang, R. Yang and G. Cui, Conjugated microporous polymers with excellent electrochemical performance for lithium and sodium storage, *J. Mater. Chem. A*, 2015, **3**, 1896–1901.

38 A. Nasser and A. E. Hendawy, Influence of HNO3 oxidation on the structure and adsorptive properties of corncob-based activated carbon, *Carbon*, 2003, **41**, 713–722.

39 T. Zhai, L. M. Wan, S. Sun, Q. Chen, J. Sun, Q. Y. Xia and H. Xia, Phosphate ion functionalized Co3O4 ultrathin nanosheets with greatly improved surface reactivity for high performance pseudocapacitors, *Adv. Mater.*, 2017, **29**, 1604167.

40 Z. H. Pu, I. S. Amiinu, C. T. Zhang, M. Wang, Z. K. Kou and S. C. Mu, Phytic acid-derivative transition metal phosphides encapsulated in N,P-codoped carbon: An efficient and durable hydrogen evolution electrocatalyst in a wide pH range, *Nanoscale*, 2017, **9**, 3555–3560.

41 H. Peng, G. Ma, K. Sun, Z. Zhang, Q. Yang and Z. Lei, Nitrogen-doped interconnected carbon nanosheets from pomelo mesocarps for high performance supercapacitors, *Electrochim. Acta*, 2016, **190**, 862–871.

42 D. W. Wang and D. S. Su, Heterogeneous nanocarbon materials for oxygen reduction reaction, *Energy Environ. Sci.*, 2014, **7**, 576–591.

43 Y. L. Wu, Y. L. Chen, H. Q. Wang, C. M. Wang, A. S. Wang, S. Zhao, X. Y. Li, D. F. Sun and J. Z. Jiang, Efficient ORR electrocatalytic activity of peanut shell-based graphitic carbon microstructures, *J. Mater. Chem. A*, 2018, **6**, 12018–12028.

44 J. T. Li, F. K. Meng, S. Suri, W. Q. Ding, F. Q. Huang and N. Q. Wu, Photoelectrochemical performance enhanced by a nickel oxide-hematite p–n junction photoanode, *Chem. Commun.*, 2012, **48**, 8213–8215.

45 J. Q. Lv, S. C. Abbas, Y. Y. Huang, Q. Liu, M. X. Wu, Y. B. Wang and L. M. Dai, A photo-responsive bifunctional electrocatalyst for oxygen reduction and evolution reactions, *Nano Energy*, 2018, **43**, 130–137.

46 J. H. Zheng and L. Zhang, Incorporation of CoO nanoparticles in 3D marigold flower-like hierarchical architecture MnCo2O4 for highly boosting solar light photo-oxidation and reduction ability, *Appl. Catal., B*, 2018, **237**, 1–8.

47 J. Masa, W. Xia, I. Sinev, A. Q. Zhao, Z. Y. Sun, S. Grützke, P. Weide, M. Muhler and W. Schuhmann, MnxOy/NC and

CoxOy/NC nanoparticles embedded in a nitrogen-doped carbon matrix for high-performance bifunctional oxygen electrodes, *Angew. Chem., Int. Ed.*, 2014, **53**, 8508–8512.

48 Y. Tong, P. Z. Chen, T. P. Zhou, K. Xu, W. S. Chu, C. Z. Wu and Y. Xie, A bifunctional hybrid electrocatalyst for oxygen reduction and evolution: Cobalt oxide nanoparticles strongly coupled to B,N-decorated graphene, *Angew. Chem., Int. Ed.*, 2017, **56**, 1–6.

49 W. Chaikittisilp, N. L. Torad, C. L. Li, M. Imura, N. Suzuki, S. Ishihara, K. Ariga and Y. Yamauchi, Synthesis of nanoporous carbon-cobalt-oxide hybrid electrocatalysts by thermal conversion of metal-organic frameworks, *Chem. - Eur. J.*, 2014, **20**, 4217–4221.

50 S. X. Yang, W. P. Zhu, Z. P. Jiang, Z. X. Chen and J. B. Wang, The surface properties and the activities in catalytic wet air oxidation over CeO2-TiO2 catalysts, *Appl. Surf. Sci.*, 2006, **252**, 8499–8505.

51 Y. B. Li and C. Zhao, Enhancing water oxidation catalysis on a synergistic phosphorylated NiFe hydroxide by adjusting catalyst wettability, *ACS Catal.*, 2017, **7**, 2535–2541.

52 Z. D. Huang, J. H. Liu, Z. Y. Xiao, H. Fu, W. D. Fan, B. Xu, B. Dong, D. Liu, F. N. Dai and D. F. Sun, A MOF-derived coral-like NiSe@NC nanohybrid: An efficient electrocatalyst for the hydrogen evolution reaction at all pH values, *Nanoscale*, 2018, **10**, 22758–22765.

53 B. Q. Li, S. Y. Zhang, B. Wang, Z. J. Xia, C. Tang and Q. Zhang, A porphyrin covalent organic framework cathode for flexible Zn–Air batteries, *Energy Environ. Sci.*, 2018, **11**, 1723–1729.